A&A 394, 1069–1076 (2002)
DOI: 10.1051/0004-6361:20021196

Astronomy & Astrophysics

2D-spectroscopic observations of *G*-band bright structures in the solar photosphere

K. Langhans, W. Schmidt, and A. Tritschler

Kiepenheuer–Institut für Sonnenphysik, Schöneckstr. 6, 79104 Freiburg, Germany

Received 10 June 2002 / Accepted 7 August 2002

Abstract. We took two-dimensional spectra with the filter spectrometer TESOS at the German Vacuum Tower Telescope, Tenerife, of an absorption line of the CH molecule and a Fe II-line in the *G*-band at 430.3 nm. We observed a region, close to disk center of the Sun, that showed a lot of structures with enhanced *G*-band intensity (up to 1.3 times the mean intensity of normal granulation). Our spectroscopic investigation of these structures suggests two classes which differ in their spectroscopic signature: (a) Bright structures caused by significant (up to 40%) weakening of absorption lines of the CH molecule; (b) bright structures only caused by an enhanced continuum intensity. In order to distinguish between those two classes we introduce a Bright Point Index (BPI) defined by the ratio of the normalized line depressions of the Fe II and the CH-line. The bright structures caused by weakening of the CH-lines have high BPI values and are accompanied by downflows. The remaining *G*-band bright structures have low BPI and are related to granules.

Key words. Sun: photosphere

1. Introduction

2D-imaging of the solar surface in the CH absorption band at 430.6 nm (*G*-band) is used as a diagnostic tool for investigation of the nature of photospheric bright points, which are interpreted as the manifestation of small-scale magnetic flux concentrations. Photospheric bright points have a much higher contrast in the *G*-band than at other wavelengths (Mehltretter 1974; Muller & Roudier 1984; Muller & Mena 1987; Berger 1997; Title & Berger 1996; Berger et al. 1998). Berger et al. (1995) find the maximum intensity of bright points to be 30% higher than the mean undisturbed photosphere. The intensity is independent of the area and morphological structure of the bright points.

Photospheric bright points are located in intergranular lanes as well as at the edges of certain bright granules. The former are co-spatial with a signal in simultaneously observed magnetograms with an angular resolution down to 0.2 arcsec, but for the latter ones there is no correlation (Berger & Title 2001).

There are several hypotheses which could explain the brightness: (i) *The CH-lines cause radiation escape somewhat higher up in the atmosphere, where the flux tubes are heated* (called *conventional wisdom* by Rutten 1999). (ii) The evacuation of the flux tube *owing to the surplus of magnetic pressure* results in a deeper view into the flux tube down to hotter layers (Sánchez Almeida & Lites 2000). Their explanation is based on LTE. (iii) The UV radiation of the surrounding hot plasma leads to an increased dissociation of CH-molecules inside the flux tube (Rutten 1999). (Literal citations are in italics).

However, these hypotheses describe only aspects of the real mechanism behind the *G*-band brightness of small-scale magnetic structures. All explanations imply a decreased CH-line depression in spectra of bright points compared to spectra of the surrounding photosphere. Langhans et al. (2001) confirm this conclusion by recording the *G*-band spectrum from 430.24 nm to 430.78 nm of isolated *G*-band bright points.

Sánchez Almeida et al. (2001) and Steiner et al. (2001) assume LTE and perform a synthesis of *G*-band spectra for different empirical models representative for network magnetic elements as well as the undisturbed Sun. Sánchez Almeida et al. (2001) compared their synthesis with observations of spectrally unresolved intensity. They find that their calculations are consistent with observations of Koutchmy (1977), de Boer & Kneer (1992), Berger et al. (1995), Berger et al. (1998), Berger & Title (1996) and Title & Berger (1996) independent on the characteristics of the model atmosphere used (flux tube or magnetic micro-structure). They also predict small magnetic elements that do not show a radiative signature in *G*-band images in accordance with observations (e.g. Berger 1997; Berger & Title 2001). Further, Sánchez Almeida et al. (2001) find that the CH photodissociation plays a minor role. The calculations of Steiner et al. (2001) show that the increased temperature of the flux tube atmosphere is able to enhance the *G*-band intensity contrast of the bright point by a factor of 3.7 in comparison to the corresponding value in the continuum (theoretical continuum at 430 nm).

Send offprint requests to: K. Langhans,
e-mail: kai@kis.uni-freiburg.de

To date, all synthesis of *G*-band spectra, done for different empirical models of flux tube atmospheres, are compared with observations that are based on imaging. With this paper we add the spectroscopic information to the discussion about the high contrast of *G*-band bright points. Sections 2 and 3 present the observations, data set characteristics and error sources, Sect. 4 presents the results, which are discussed in Sect. 5.

2. Observations and data reduction

2.1. Specification of the absorption lines

The *G*-band consists mainly of electronic transitions between rotational and vibrational sublevels of the CH-molecule. Furthermore it contains several atomic lines. The high line density results in the absence of a real continuum in the whole band and restricts the line selection for a spectroscopic investigation of *G*-band bright structures.

We observed two nearby lines of Fe II and CH for this investigation. As a representative for the CH-molecule we select the line at 430.34 nm, which belongs to the rotation branch "*Q*" with quantum number 16 and to the vibration band 1–1. The second selected line is the Fe II-line at 430.32 nm, multiplet number 27. The ionic iron line is suitable for comparison, because the partial density of Fe II remains practically constant over a large temperature range of commonly-used quiet Sun and flux tube models. (See Steiner et al. 2001, and Sect. 4.3).

The "continuum" intensity between the two lines, at a wavelength of 430.33 nm, does not reach the true continuum level, due to the overlap of the line wings. A comparison with a photospheric spectral atlas (Delbouille et al. 1990) gives the relative intensity $I_{\rm atlas} = 0.895$. We use $I_{\rm atlas}$ as a normalization factor for our spectra.

The CH-line is free of blends, while the Fe II-line is blended by a CH-line in the blue wing (430.31 nm, rotation branch "*R*", quantum number 1, vibration band 1–1). This blend influences the accuracy of the determination of both, the Fe II-line core position and the Fe II-line depression. A correct investigation of the influence of the blend is difficult because of the absence of a real continuum. To carry out an estimation, we fit the atlas profile of the blended Fe II-line by a double Gaussian. A reduction of the line depression of the blend by 20% reduces the Fe II-line depression by 2.8% and shifts the Fe II-line core by 0.18 pm, which corresponds to a velocity shift of 126 $\mathrm{m\,s^{-1}}$. (All spectral data were taken from Moore et al. 1966).

2.2. Observations

The observations have been carried out at the German Vacuum Tower Telescope in the Observatorio del Teide, Tenerife, on August 4, 2001. We used the filter spectrometer TESOS (Kentischer et al. 1998; Tritschler et al. 2002) to take two-dimensional spectra of a pore and its immediate surroundings. The telescope was pointed at heliographic position S 8.3° W 3.3°. The field of view is 30×30 arcsec^2. TESOS was used in its high-resolution mode with a pixel size of 0.089 arcsec and a spectral resolution of 300 000. A single data set consists of 34 narrow-band filtergrams taken at equidistant positions across the two selected spectral lines. The wavelength step width was 1.62 pm. A 0.89 nm (*FWHM*) bandpass filter centered at 430.6 nm was used as a prefilter for the filtergram channel. Broadband images with exactly the same field of view were recorded simultaneously with each filtergram using a 0.39 nm (*FWHM*) band-pass filter centered at 431.1 nm. Due to the recently installed backside-illuminated cameras an exposure time of 250 ms was possible, resulting in a measurement cadence of 17 s for the whole scan. During a short period of fair to good seeing we obtained one scan of good (i.e. constant) quality. Our analysis is based on this scan. The observation time was 10:27 UT. The granular rms-intensity contrast varied around 6% (see Sect. 3.2), the spatial resolution is estimated to be about 0.5 arcsec.

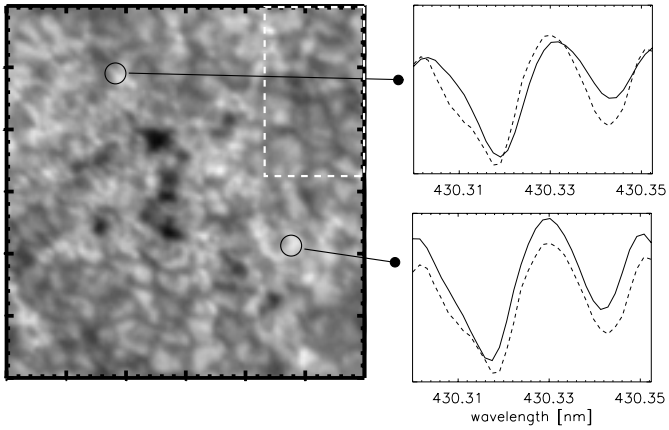

Fig. 1. Left: *G*-band broadband channel at 431.1 nm. The framed area marks the reference, a region of "normal" granulation. One tickmark represents 1 arcsec. Right: examples of spectra of two bright structures with different spectroscopic signatures. The solid curves correspond to the marked structures. The dashed curves show the spectrum averaged over the "reference region".

Dark current subtraction and flat field corrections are done for each wavelength position separately. The orientation and the image scale of the broadband channel are adapted to that of the filtergram channel. A rigid alignment of the individual filtergrams within the scan was done with respect to an average of the 5 best broadband images during the scan.

2.3. Methods to determine the line core positions and line shift

We applied two different methods for line shift determination: (i) *Fourier method:* This method, described by Schlichenmaier & Schmidt (2000), is convenient for symmetric lines and is very insensitive to noise. The calculated line shift is comparable to a center-of-gravity shift. (ii) *Polynomial fit to the line core:* This method uses a least-squares second order polynomial fit in order to determine the line core shift. The resulting velocities originate from higher photospheric layers.

For the Fe II-line only the last method is applicable, because of the CH-blend.

3. Data quality and error estimation

3.1. Spectral resolution

Figure 2 shows the observed spectral lines. The "+"-symbol corresponds to the mean spectrum of normal granulation in the data set. The spectrum represented by the "△"-symbol is based on the atlas profile, adapted to the spectral resolution of TESOS. The distance between two "△"-symbols corresponds to the selected step size used for the observations. The comparison between the observed and the "simulated" profile demonstrates the high spectroscopic quality of our *G*-band data.

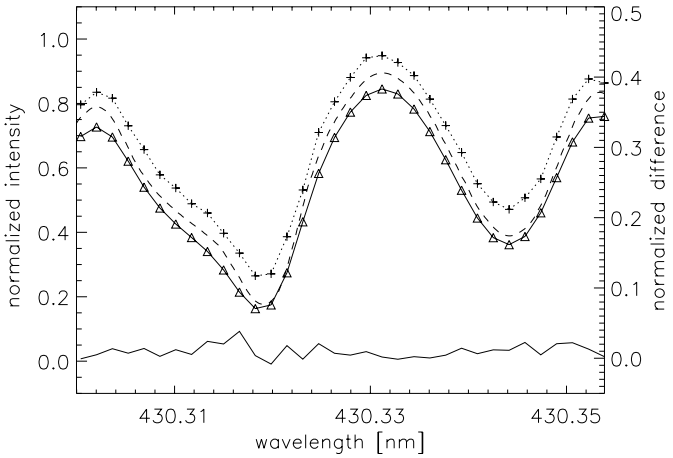

Fig. 2. "+" represents the observed profile, "△" the "simulated" profile and the dashed curve the atlas spectra. For clarity the observed data is shifted by +0.05 and the simulated data by –0.05 intensity units. The curve below represents the normalized difference $(I^{+} - I^{\triangle})/(I^{+} + I^{\triangle})$ of the data and the simulation (scale to the right).

3.2. Seeing effects

TESOS obtains 2D-spectra by scanning through the spectral line. Since the images are not taken simultaneously the line profiles are influenced by seeing effects. As described by Schlichenmaier & Schmidt (2000), the variable seeing conditions can induce shifts of the line profiles. This is a potential error source when calculating e.g. velocity maps from the data. Figure 3 shows the rms-intensity contrast for the broadband channel during the scan as a function of time. The rms-intensity contrast is calculated in each frame in a region of normal granulation, located in the upper right corner of the field of view, as indicated in Fig. 1. The contrast is varying between 5 and 6.8% (rms). On average the seeing conditions during the Fe II-line scan are better than for the CH-line scan. To estimate the errors, we produce a synthetic filtergram scan, I^{i}_{syn}, making use of the simultaneously observed broadband images and a mean line profile, based on the filtergrams. For each step i we multiply the broadband image, I^{i}_{bb}, with the quotient of mean

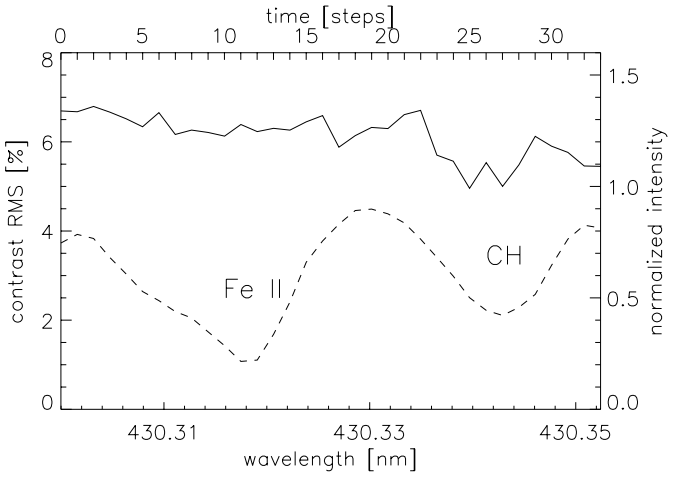

Fig. 3. The solid curve represents the course of rms-intensity contrast of normal granulation (see Fig. 1) in the broadband channel during the scan. The dashed line shows the mean intensity in normal granulation of the filtergram channel. The given wavelength range corresponds to the 34 steps of the scan.

filtergram intensity $\left\langle I^{i}_{\mathrm{nb}} \right\rangle$ and mean broadband intensity $\left\langle I^{i}_{\mathrm{bb}} \right\rangle$, each calculated for the region of normal granulation:

$$I^{i}_{\mathrm{syn}} = I^{i}_{\mathrm{bb}} \cdot \frac{\left\langle I^{i}_{\mathrm{nb}} \right\rangle}{\left\langle I^{i}_{\mathrm{bb}} \right\rangle} \quad i = 0, ..., 33,$$

where brackets denote spatial average over the "reference region" as indicated in Fig. 1. In this way, we replace the original observed line profile at each spatial position by a spatially unresolved "synthetic" line profile. This scan does not bear any physical information, like line shifts due to flows on the solar surface, but only the mean line profile weakened or strengthened by the varying intensity of the broadband image due to seeing.

In a next step we calculate maps (line core intensity, velocity, etc.) from this synthetic scan. An example of a resulting error map is shown in Fig. 4 to the right. The image visualizes the error due to seeing for the velocity map (Fe II-line, Fourier method). In the example the rms-value of the map is 26 m s^{-1} and the maximum deviation amounts to 215 m s^{-1} (peak-to-peak). The spatial error is not distributed homogeneously. However, the rms-value of these maps provides a good estimation of the error due to seeing variation. Compared to the seeing error, numerical errors – as they occur e.g. at line shift determination – are negligible. In the following analysis we give the 2σ-level based on this rms-calculation.

4. Results

4.1. Velocity maps

The CH-line is suitable for both methods of line shift determination as described in the previous section. The calculated error map gives a rms-value of 25 m s^{-1} for the map based on Fourier method and a maximum deviation of 215 m s^{-1} (peak-to-peak). The corresponding values for the map based on the

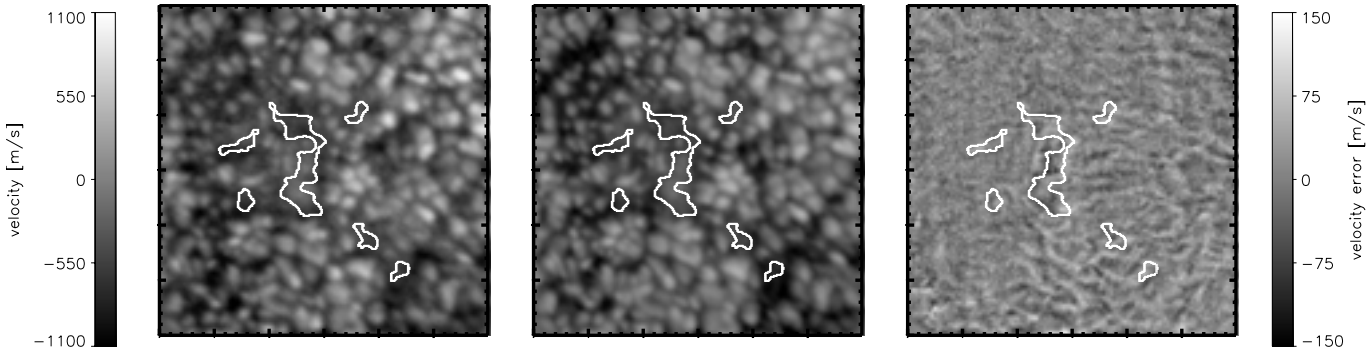

Fig. 4. Velocity maps. From left to right: map based on CH-line shift determination (Fourier method), map based on Fe II-line shift determination (polynomial fit around line core), map of seeing error for the map based on Fe II-line shift determination. The contour lines mark $I = 0.58 \cdot \langle I_{G-\mathrm{band}} \rangle$ and indicate the location of the pores.

line-core shift are 45 m s^{-1} and 260 m s^{-1}. The maps do not differ significantly from each other.

Figure 4 shows the calculated velocity maps for the CH-line based on the Fourier method to the left, for the Fe II-line based on the polynomial fit in the middle and the corresponding error map to the right. In the maps upflows (blue-shifts) are always represented by bright areas and related to positive velocities. The CH-map shows the same flow pattern as the Fe II-map, but it is more diffuse. This can be explained by the inferior seeing quality during the CH-line scan. The correlation coefficient of the two maps is 0.94. The rms-value of the normalized difference of the maps $(v_{\mathrm{CH}} - v_{\mathrm{Fe}})/(v_{\mathrm{CH}} + v_{\mathrm{Fe}})$ is about 0.05.

The velocity maps reproduce well the granulation pattern outside the pore in regions of normal granulation. For comparison between the velocity map and broadband or continuum filtergrams see also Fig. 5. There is a conspicuous downflow pattern in regions of abnormal granulation, which clearly differs from the downflows of the intergranular lanes in regions of normal granulation in the upper right corner of the image. These downflows form a connected area which coincides with the region of abnormal granulation and which contains most of the structures that are related to enhanced intensity in the G-band image.

4.2. Intensity maps

Figure 5, panels d and e show the line core intensity of the CH respective the Fe II-line, normalized to the local continuum. The values for the local continuum are taken from the average of the two filtergrams positioned in the neighborhood of the continuum at 430.33 nm (see Fig. 2 or Fig. 3). The line core intensities for each position are given by the minimum value of the polynomial fit, fitted around the profile minimum.

In both maps, regions of enhanced line core intensity outline the intergranular lanes. However, the line core intensity of CH behaves slightly differently. The line core intensity of the CH-line is partially much more enhanced than the line core intensity of the Fe II-line. Away from the pore, the increased line core intensity of the CH-line is restricted to the intergranular lanes. Close to the pore, the brightenings expand in space and cover larger areas that do not show any structure.

In the following we use the term "G-band brightness" (see Berger et al. 1998) for the normalized intensity of the broadband channel at 431.1 nm. The G-band contrast is then defined by

$$C_{G-\mathrm{band}} = \frac{I_{\mathrm{bb}}}{\langle I_{\mathrm{bb}} \rangle} - 1.$$

4.3. Bright point index

Langhans et al. (2001) show that bright points can be characterized spectroscopically by a decreased line depression of the CH absorption lines, whereby the line depression of the atomic lines within the observed spectral range (430.24 nm to 430.78 nm) remain almost unchanged.

To distinguish regions where CH-line depression dominates from regions where both lines or only the Fe II-line is depressed, we introduce the "Bright Point Index" (BPI). The index is defined as the ratio of the relative line depression of the Fe II and the CH-line, minus one:

$$\mathrm{BPI} = \frac{I_{\mathrm{cont}} - I_{\mathrm{lc}}^{\mathrm{Fe}}}{\left\langle I_{\mathrm{cont}} - I_{\mathrm{lc}}^{\mathrm{Fe}} \right\rangle} \cdot \frac{\left\langle I_{\mathrm{cont}} - I_{\mathrm{lc}}^{\mathrm{CH}} \right\rangle}{I_{\mathrm{cont}} - I_{\mathrm{lc}}^{\mathrm{CH}}} - 1.$$

For this calculation all intensities are normalized to I_{atlas}. I_{cont} corresponds to the "continuum" intensity at 430.33 nm.

Through the use of a low-excitation majority-stage ionic iron line in combination with a CH-line of similar strength, the BPI provides a measure of CH-abundance variations; it is nearly free of direct temperature effects on the line source functions. (A large BPI corresponds to low CH-abundance.) The BPI map is shown in Fig. 5d. The regions of increased CH-line core intensity and unchanged Fe II-line core intensity are emphasized. Regions where both lines are depressed in the same way make a smaller contribution to the BPI map compared to the contribution to the maps of line core intensity.

The correlation diagrams in Fig. 6 show the BPI versus the line depression of both absorption lines. The error ellipsoids in one of the lower corners of the diagrams (and in all following correlation diagrams) represent the 2σ-confidence level for each data point, which results from the calculation of the rms-values of the concerning error maps as discussed in Sect. 3.2. For clarity in Fig. 6 only data points for a threshold

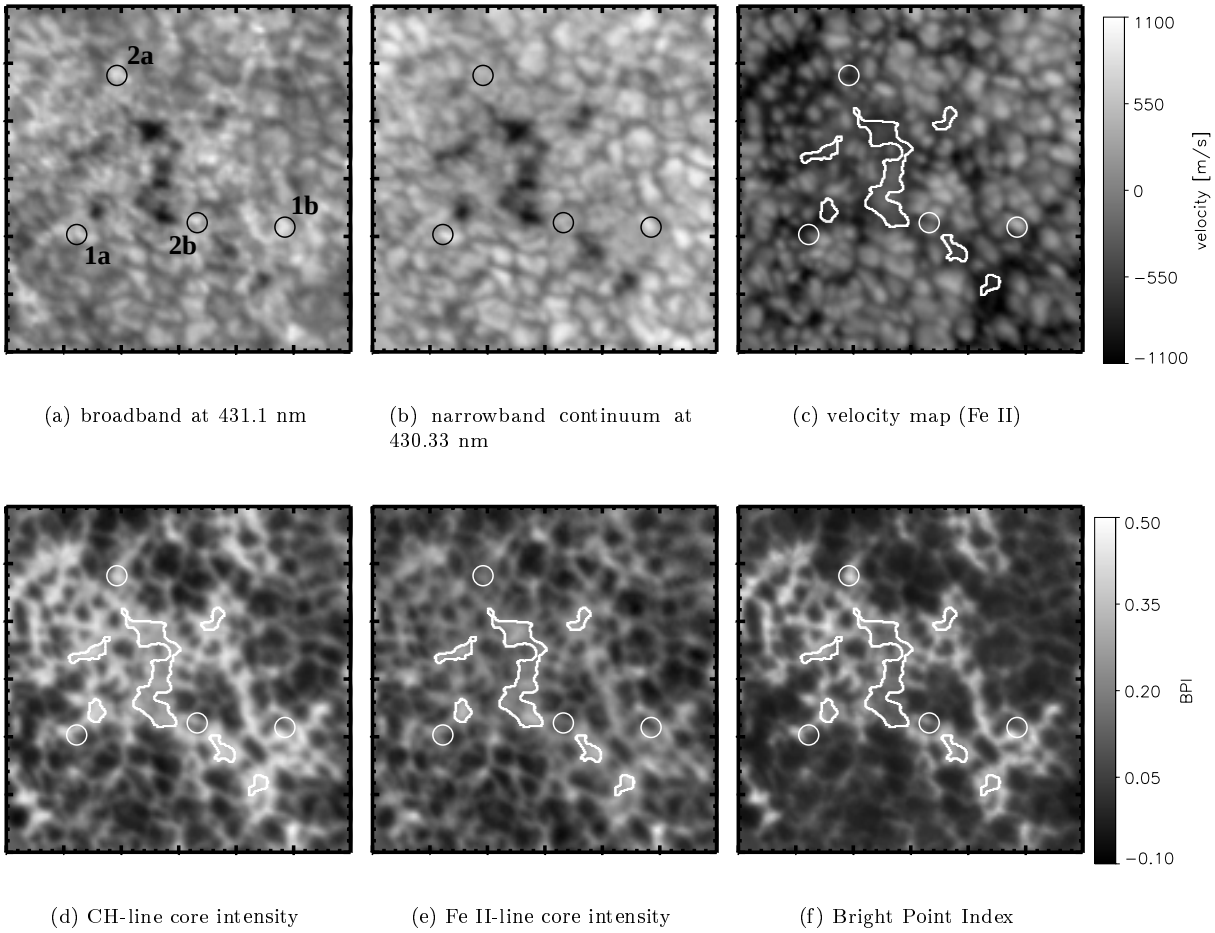

(a) broadband at 431.1 nm (b) narrowband continuum at 430.33 nm (c) velocity map (Fe II)

(d) CH-line core intensity (e) Fe II-line core intensity (f) Bright Point Index

Fig. 5. Intensity and velocity maps. The circles mark the examples, that are described in Sect. 4.4.

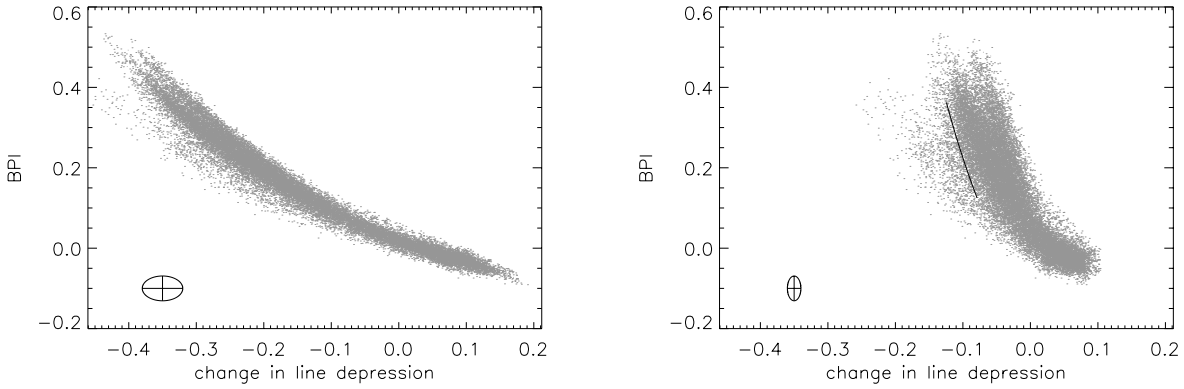

Fig. 6. Relation between BPI and change in line depression. For clarity only data points for a threshold *G*-band contrast ≥10% are taken into account. The error ellipsoids indicate the 2σ-level for each data point. Left CH-line, Right: Fe II-line, the inclined line in the plot indicates the expected effect on the BPI and line depression of the Fe II-line by the CH-blend.

G-band contrast ≥10% are considered. Thus, the large contribution from granules with a brightness ≤1.1 $\langle I_{\rm bb}\rangle$ are excluded in the correlation diagrams of Fig. 6 and some following figures. To estimate how the CH-blend in the blue wing of the Fe II-line affects the BPI, we vary the strength of the blend in the double Gaussian representing the blended Fe II-line as described in Sect. 2.1. The resulting values for the BPI are represented by the inclined line in the Fe II-diagram. In the case of a decreased CH-abundance the corrected BPI is higher than the BPI for the uncorrected case. Therefore we do not correct the BPI for the CH-blend in the following calculations.

4.4. G-band bright structures?

We use the BPI to separate *G*-band bright structures in two classes: (a) structures which are bright, due to a significant difference in CH and Fe II line depression; (b) structures which are bright due to an increase of the local continuum intensity. Examples of these structures are marked by circles in Fig. 5.

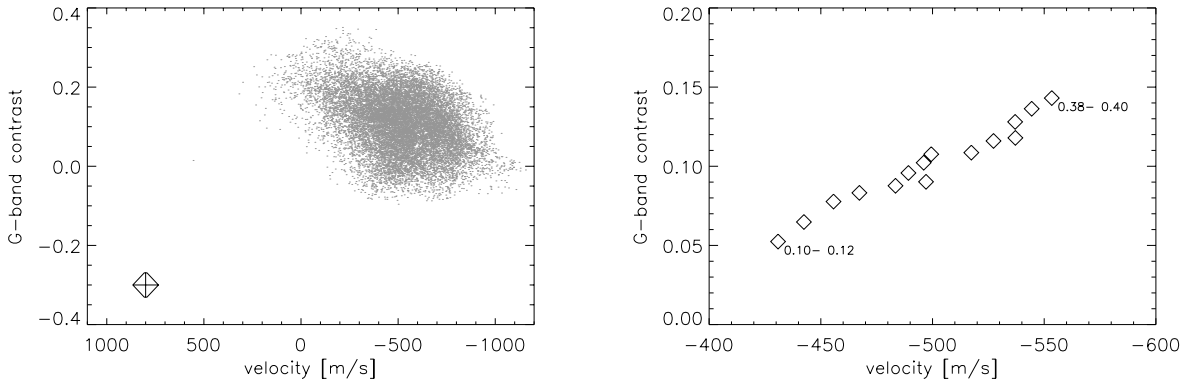

Fig. 7. Correlation diagrams: *G*-band contrast vs. flow velocity. Left: Criterion of data point selection is a BPI above 0.2. Right: center-of-gravity plot. The small numbers indicate BPI intervals to the corresponding center-of-gravity, indicated by "◇".

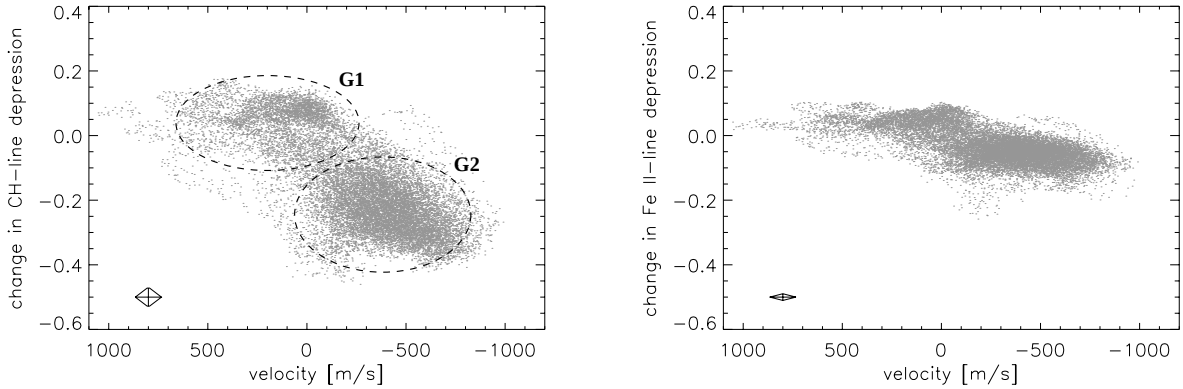

Fig. 8. Correlation diagrams: change in line depression vs. flow velocity. Criterion of data point selection is an enhanced *G*-band brightness ($C_{G-\mathrm{band}} \geq 0.1$). Left: CH-line, G1 and G2 are explained in Sect. 4.5. Right: Fe II-line.

All features appear bright in the *G*-band image (TESOS broadband channel). Examples 2a and 2b are not conspicuous neither in the narrowband continuum image nor in the line core intensity map of Fe II. The line core intensity of CH is high, which leads to a high BPI-value as well. The dopplergram shows that the selected structures are located in downflow regions. In contrast thereto, the *G*-band structure of the examples 1a and 1b coincides with high intensity in the narrowband continuum image and low line core intensities in Fe II and CH as well. The BPI is accordingly low. The flow map shows a slight upflow. The spectra of the examples (1b, 2a) are plotted in Fig. 1.

4.5. Correlations

In Sect. 4.4 we described the relation between the *G*-band brightness, the Doppler velocity and the BPI for different structures. In this Section we follow a quantitative approach using correlation diagrams. Data points from the pores are excluded by requiring $I \geq 0.58 \cdot \langle I_{G-\mathrm{band}} \rangle$; the mask is marked by contour lines in all but the continuum maps.

In the left diagram of Fig. 7 all data are plotted with a BPI $\geq$ 0.2. All points are related to relatively high *G*-band brightness ($-0.1 \leq C_{G-\mathrm{band}} \leq 0.3$) and downflows. Next we sort the data into bins of 0.02 BPI units and calculate the center-of-gravity for each bin. (Only intervals with more than 200 data points were used.) The result is shown in the right panel of Fig. 7: The BPI is directly correlated with the downflow velocity of the corresponding areas (pixels).

We also use a different approach starting from the *G*-band brightness to investigate the relation of the percentage change of line depression and the Doppler velocity. The "change of line depression" $(I_{\mathrm{cont}} - I_{\mathrm{lc}}) / \langle I_{\mathrm{cont}} - I_{\mathrm{lc}} \rangle$ is equivalent to the later defined line core contrast. Due to the different line strength the "change of line depression" is a more suitable measure to compare the CH- and Fe II-line. Figure 8 displays the correlation diagram for the CH-line (left) and for the Fe II line (right). In both figures all data points with an enhanced *G*-band brightness ($C_{G-\mathrm{band}} \geq 0.1$) are plotted. In the diagram for the CH-line the points are spread over a large range of velocity and over a large range in the line depression as well. As indicated in the diagram, two groups become apparent: one related to slightly increased line depression and weak upflows (G1), the second one related to downflows and a large decrease in the line depression (G2). The latter one is consequently related to higher BPI values. The corresponding diagram for the Fe II-line shows a different behavior for the same data points. The distribution of velocity is the same, but there is virtually no variation of the line depression. The examples 1a, 1b, 2a and 2b, as described in Sect. 4.4, belong to G1 and G2 respectively.

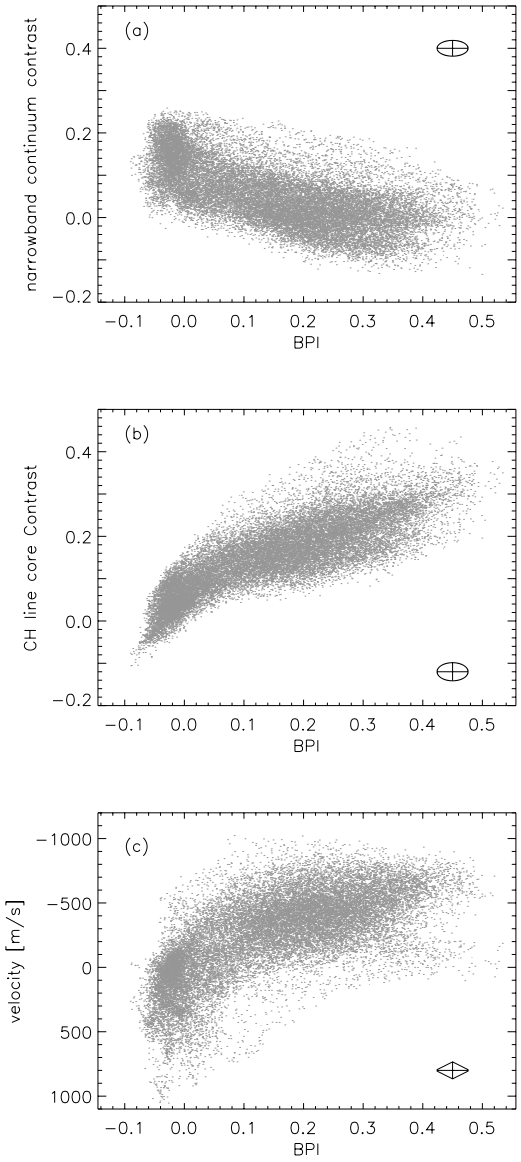

Fig. 9. Correlation diagrams. Criterion of data point selection is a *G*-band contrast ≥ 0.1. **a)** Continuum contrast vs. BPI. **b)** CH-line core contrast vs. BPI. **c)** flow velocity vs. BPI.

The *G*-band brightness is obviously caused by different effects. The brightness of G2 is clearly a line effect while the brightness of G1 is caused by an enhanced continuum intensity. The BPI for points in G1 is close to zero.

Figure 9 shows the relation of the BPI to the narrowband continuum contrast $C_{\mathrm{nb-cont}}$ and the CH-line core contrast C_{CH}. Analogous to the *G*-band contrast $C_{G-\mathrm{band}}$ we define the narrowband continuum contrast

$$C_{\mathrm{nb-cont}} = \frac{I_{\mathrm{cont}}}{\langle I_{\mathrm{cont}} \rangle} - 1,$$

where I_{cont} refers to the continuum at 430.33 nm. Additionally we define the CH-line core contrast by

$$C_{\mathrm{CH}} = \frac{I_{\mathrm{lc}}^{\mathrm{CH}}}{\left\langle I_{\mathrm{lc}}^{\mathrm{CH}} \right\rangle} - 1.$$

For all correlation diagrams in Fig. 9 only data points are plotted that are related to enhanced broadband intensity ($C_{G-\mathrm{band}} \geq 0.1$). The correlation diagram in Fig. 9a shows $C_{\mathrm{nb-cont}}$ versus BPI, Fig. 9b C_{CH} versus BPI and Fig. 9c the velocity versus BPI. All diagrams show a concentration of data points for BPI values around zero. For these points the ratio of line depression is more or less the ratio calculated for the mean profiles of the reference region. They belong to G1 as indicated in Fig. 8, because they show a CH line core contrast around zero. Moreover, they show an enhanced continuum contrast and are related to flow velocities around 0 m s^{-1} or slight upflows. Towards higher values of BPI the diagrams show different correlations: The continuum contrast decreases slightly, the CH-line core contrast increases and the flow velocity changes toward downflows.

5. Discussion

The evaluation of the 2D-spectra and the simultaneously taken broadband images show that the commonly called *G*-band bright points are characterized spectroscopically by an increased line core intensity of the CH absorption lines. They are embedded in regions that still show enhanced line core intensity of the CH-lines in comparison to the quiet Sun.

Our observations suggest to classify *G*-band bright structures by their spectroscopic signature. The defined BPI is a suitable tool to quantify the spectroscopic signature of *G*-band bright structures. A high value of the BPI, corresponding to a decreased line depression of the CH in comparison to the Fe II-line, characterizes *G*-band bright structures with an enhanced *G*-band contrast and is related to the downflow regions of the intergranular lanes. Their brightness is caused by significant weakening of the CH-absorption line. The remaining *G*-band bright structures show a low BPI and a lower CH line core contrast, but an increased contrast in the narrow band continuum. They are related to granules and do not to show a downflow. Their brightness is caused by enhanced continuum intensity.

The presented results confirm and complement former observations (Langhans et al. 2001). The BPI provides an identification method for *G*-band bright structures from the spectroscopic viewpoint. The statistics of our data set shows that the BPI is a reliable criterion for the identification.

To our knowledge no simultaneously observed magnetograms are available for the data presented here. But it seems reasonable to suppose that our spectroscopic distinction of *G*-band bright structures, by analysis of the BPI and the flow, is identical to the classification in magnetic and non-magnetic sub-arcsecond structures done by Berger & Title (2001). Berger & Title (2001) find that bright points that are co-spatial with magnetic fields, are located in intergranular lanes and the non-magnetic ones at the *edges of certain bright rapidly expanding granules*. Concerning the location, this distinction matches with the measured flows. Berger & Title (2001) find that within the best spatial resolution of their magnetograms (∼0.3 arcsec) *all G-band bright points, properly distinguished from granulation brightening, are magnetic in nature.*

Assuming LTE and a similar formation height for the Fe II- and the CH-line, we can identify the brightness temperature,

obtained from the measured absolute intensity in the Fe II-line core, with the temperature at $\tau = \mu = 1$. An unchanged Fe II-line core intensity within a *G*-band brightening implies that the enhanced CH-line intensity is most likely not due to a direct temperature effect – be it through the line source function or through enhanced dissociation of CH. Consequently the CH dissociation must be caused by different mechanisms, like hot wall radiation. Our observations do not contradict this explanation, but further observations at higher spatial resolution and under constant seeing conditions are required to confirm this hypothesis.

Acknowledgements. J. Bruls provided very useful hints and comments. One of us (K.L.) is supported by the Deutsche Forschungsgemeinschaft.

References

Berger, T. E. 1997, Ph.D. Thesis Stanford University
Berger, T. E., Loefdahl, M. G., Shine, R. S., & Title, A. M. 1998, ApJ, 495, 973
Berger, T. E., Schrijver, C. J., Shine, R. A., et al. 1995, ApJ, 454, 531
Berger, T. E., & Title, A. M. 1996, ApJ, 463, 365
Berger, T. E., & Title, A. M. 2001, ApJ, 553, 449
de Boer, C. R., & Kneer, F. 1992, A&A, 264, L24
Delbouille, L., Roland, G., & Neven, L. 1990, Atlas photométrique DU spectre solaire de λ 3000 Å à λ 10000 Å (Liège: Université de Liège, Institut d'Astrophysique, 1990)
Kentischer, T. J., Schmidt, W., Sigwarth, M., & Uexkuell, M. V. 1998, A&A, 340, 569
Koutchmy, S. 1977, A&A, 61, 397
Langhans, K., Schmidt, W., Rimmele, T., & Sigwarth, M. 2001, in Advanced Solar Polarimetry – Theory, Observation, and Instrumentation, ASP Conf. Ser., 236, 439
Mehltretter, J. P. 1974, Sol. Phys., 38, 43
Moore, C. E., Minnaert, M. G. J., & Houtgast, J. 1966, The solar spectrum 2935 Å to 8770 Å (National Bureau of Standards Monograph, Washington: US Government Printing Office (USGPO)
Muller, R., & Mena, B. 1987, Sol. Phys., 112, 295
Muller, R., & Roudier, T. 1984, Sol. Phys., 94, 33
Rutten, R. J. 1999, in Third Advances in Solar Physics Euroconference: Magnetic Fields and Oscillations, ASP Conf. Ser., 184, 181
Sánchez Almeida, J., & Lites, B. W. 2000, ApJ, 532, 1215
Sánchez Almeida, J. S., Ramos, A. A., Trujillo Bueno, J., & Cernicharo, J. 2001, ApJ, 555, 978
Schlichenmaier, R., & Schmidt, W. 2000, A&A, 358, 1122
Steiner, O., Hauschildt, P. H., & Bruls, J. 2001, A&A, 372, L13
Title, A. M., & Berger, T. E. 1996, ApJ, 463, 797
Tritschler, A., Schmidt, W., Langhans, K., & Kentischer, T. J. 2002, Sol. Phys., in press